Article

Correlation of Bone Textural Parameters with Age in the Context of Orthopedic X-ray Studies

Paweł Kamiński [1,2], Rafał Obuchowicz [3,*], Aleksandra Stępień [4], Julia Lasek [5], Elżbieta Pociask [4] and Adam Piórkowski [4]

[1] Clinic of Locomotor Disorders, Andrzej Frycz Modrzewski Krakow University, 30-705 Krakow, Poland
[2] Małopolska Orthopedic and Rehabilitation Hospital, Modrzewiowa 22, 30-224 Krakow, Poland
[3] Department of Diagnostic Imaging, Jagiellonian University Medical College, Kopernika 19, 31-501 Krakow, Poland
[4] Department of Biocybernetics and Biomedical Engineering, AGH University of Science and Technology, 30-059 Krakow, Poland
[5] Faculty of Geology, Geophysics and Environmental Protection, AGH University of Science and Technology, 30-059 Krakow, Poland
* Correspondence: rafalobuchowicz@su.krakow.pl

Abstract: The aim of this study was to establish a relationship between the textural parameters observed in X-ray images of bones and the age of the individual. The study utilized a meticulous visual analysis of the images to identify significant correlations between textural features and age. Five distinct regions of interest, namely the Wing of the Ilium, Neck of the Femur, Greater Trochanter, Ischium, and Shaft of the Femur, were identified on both sides of the body. Textural parameters were then measured for each of these regions. The left femoral neck showed the most noteworthy associations, with the textures generated from the histogram of oriented gradients and gray-level co-occurrence matrix exhibiting the strongest correlations (ρ -0.52, *p*-value 4.95×10^{-14}). The main finding of the current study is that correlation of age-dependent bone structure differences in the femoral neck area is higher than in other structures of the femur. This proposed methodology has the potential to aid in the early detection of osteoporosis, which is crucial for devising treatment plans and identifying potential risks associated with bone fragility.

Keywords: textural analysis; X-ray; radiographs; bone age; bone aging; osteoporosis

1. Introduction

Bone is a complex composite formed from both organic and inorganic components. It serves as a supportive tissue that evolved to provide a great advantage for land animals, despite being energy-consuming. From a mechanical point of view, bone tissue must possess maximal strength and stiffness (resistant to failure and deformation) with the lowest possible mass. Therefore, it has a complex internal organization, with an outer cortical zone and an internal trabecular bone [1]. This three-dimensional architecture enables it to withstand tension and compression forces that can be effectively dissipated throughout the bone without producing mechanical damage [2]. To fulfill the mechanical needs of the skeleton as a supportive tissue, bone is organized hierarchically with compact bone (approximately 80% of the skeleton) and trabecular or spongy bone (20% of the skeleton) [3]. At the microstructure level, bone is composed of osteons, which are longitudinal canals called Haversian canals surrounded by lamellae [1]. The Haversian canals house osteoblasts and blood vessels, and they are about 20 to 100 μm in diameter [4]. Single lamellae are up to 7 μm thick and up to 25 μm long. These are the locations where the inorganic phase responsible for the mechanical properties of the bone is accumulated. The inorganic phase consists of apatite-like mineral hydroxyapatite crystals ($Ca_{10}(PO_4)_6(OH)_2$) [3], which have a hexagonal lattice structure and are formed as plates with an average size of $50 \times 25 \times 3$ nm.

These structures are adjacent to collagen I, an organic material formed from protein material oriented parallel to the long axis of the bone [5]. The presence of inorganic structures embedded in collagen fibrils is responsible for the interaction with electrons emitted from the anode of the X-ray lamp [6]. Collisions with inorganic materials absorb electron energy, which is responsible for the projection of the bone, detectable by the visual system. The spatial resolution of the X-ray picture is high. For a 35 × 43 cm cassette and a 20 × 24 cm cassette, three and five line pairs per millimeter are reported, respectively [7]. The range of dimensions of bone structure accessible by X-ray imaging is up to 5 μm, which corresponds to the bone microstructure.

Osteocytes are residual, long-lived bone cells that are interconnected with each other with processes and form an important signaling network, which serves as mechanosensory units directing the response of osteoclasts-bone-depleting cells and osteoblasts-bone-forming cells [8]. Cellular action serves in constant longitudinal and transverse remodeling of the bone, where matrix turnover makes complete matrix exchange every 10 years [9]. The process of mineral exchange serves adjustments to the specific loads of the bone excreted by physical activity, but also the metabolic needs of the organism as the skeleton is a reservoir of calcium ions and takes part in the interchange of inorganic substances with the extracellular fluid (ECF) [10]. Bone turnover is precisely regulated by hormonal action throughout life, which is one of the causative factors of the differences between the skeletal systems of women and men observed from puberty to older age [11]. Pathologic changes in the regulatory process include an increase in cortical porosity, trabecular thinning, and a decrease in trabecular interconnections [12]. This normal process of bone degeneration can be markedly increased if the control of bone metabolism is dysregulated. Moreover, of importance are physical activity and dietary habits, including alcohol and calcium product consumption, but also the presence of diseases impacting hydrogen ions and calcium/phosphorus equilibrium [13–15].

It is worth noting that vitamin D and calcium deficiency may lead to secondary hyperparathyroidism, which promotes osteoclastic activation with an increase in calcium bone to extracellular fluid conversion [16]. The most important recognized regulatory factor is linked to estrogen action, which is involved in the control of bone resorption, as it inhibits osteoclast activation [17]. The processes controlling bone are very complex, and deterioration of bone architecture weakens the bone, making it susceptible to overload and a potential cause of bone trauma. Therefore, meticulous determination of the status of the bone is important at the early stages.

In the theoretical introduction above, we wish to point out that there are biology-based reasons for investigating how bone age, and hence changes in its composition and physical properties, correlate with changes in the X-ray image detectable by textural analysis. This study investigated the relationship between the textural parameters determined on the basis of radiographs of the hip bone and the age of the patients.

2. Materials and Methods

2.1. Dataset

The initial dataset comprised 3782 radiographic images of the hip and knee regions, captured using an X-ray machine and stored in PNG8 format with 8-bit color depth. The images were acquired from a group of 241 individuals of both sexes, with ages ranging from 26 to 91 years. Following an initial screening, all radiographs that did not portray the hip joint bones were excluded from the subsequent analysis. The images depicting the hip joint were obtained prior to endoprosthesis surgery or in a condition indicating the need for reoperation. In addition, images with artifacts from elements such as the mattress or endoprosthesis were also excluded. Finally, 481 radiographs from 132 patients were used for analysis, where 93 patients had a longitudinal study (several X-rays taken at intervals), and 39 patients had a single study (having only one image at one time point).

2.2. Data Acquisition

In the study X-ray machine, Del Medical EV-650, manufactured in 2008, was used. The X-ray machine was supplied with a cassette feeder (Poersch Metal Manufacturing Co., Chicago, IL 60624, USA), a portable detector DFMTS equipped with exposure tube C52 Super with an X-ray lamp RTM 101 HS manufactured by I.A.E Spa. The system is powered by a high-voltage generator (Via Sistemi Medicali). Lamp usage is carefully monitored, and the system was equipped with a new X-ray lamp (2015). System equipped with a valid technical passport to assure patient safety.

2.3. ROI Annotation

To annotate the ROIs (Regions of Interest) on the preselected images, the qMaZda software (release version 19.02) was used [18]. In each radiograph, rectangular ROIs were selected to correspond to specific anatomical structures. Where endoprostheses were present, the ROIs were refrained from being marked, resulting in a lower number of analyzed areas. A detailed description of the ROI delineation process is provided in Figure 1 and Table 1.
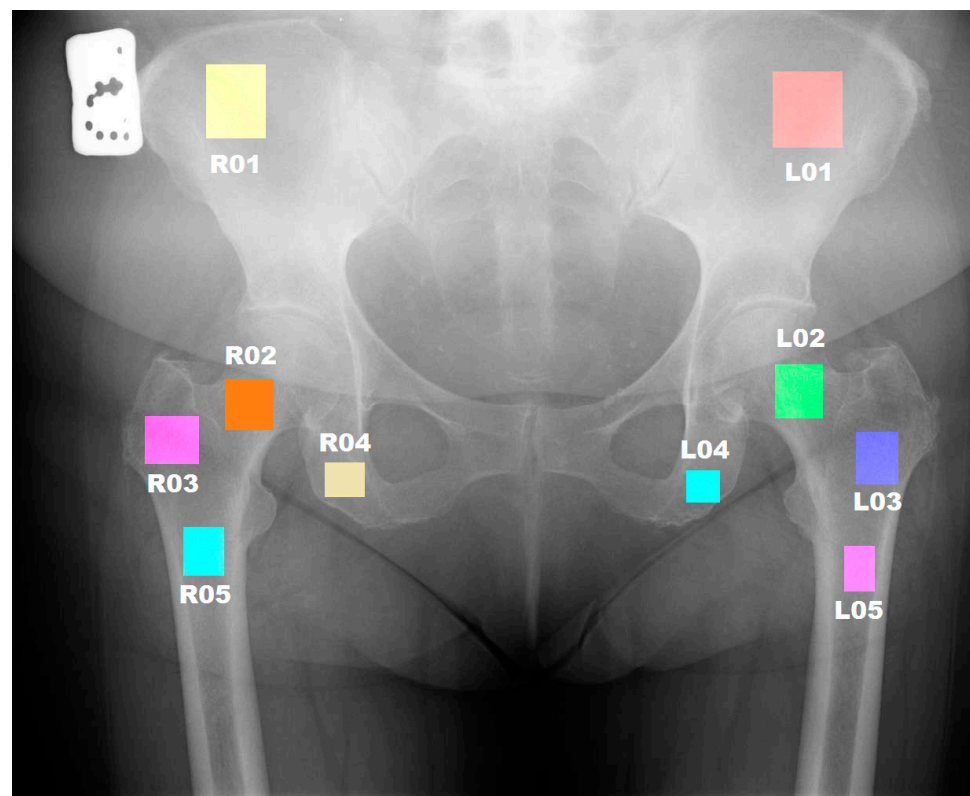

Figure 1. Regions of interest are depicted on the radiograph.

Table 1. Table of ROIs with corresponding anatomical areas.

ROI	Anatomical Structure
L 01	Wing of ilium—left side
L 02	Neck of femur—left side
L 03	Greater trochanter—left side
L 04	Ischium—left side
L 05	Shaft of femur—upper left side
R 01	Wing of ilium—right side
R 02	Neck of femur—right side
R 03	Greater trochanter—right side
R 04	Ischium—right side
R 05	Shaft of femur—upper right side

2.4. Textural Analysis

Texture analysis is a type of image processing that examines image patterns and structural features. It calculates the various statistical measurements of the grey-level intensity values of the pixels in the image and can provide information on the spatial distribution and arrangement of those pixels. Textural analysis can be used to extract contrast, entropy, and homogeneity, which express subtle changes in the X-ray image and reflects different bone tissue organization [19].

The textural analysis for each ROI was also carried out using qMaZda software, which provides a plethora of different textural parameters. The qMaZda software computes multiple textural features, including histogram-based, co-occurrence-matrix-based, run-length-matrix-based, gradient-map-based, autoregressive model-based, and Haar wavelet transform-based features. All these parameters can be calculated directly from the original image histogram or based on a normalized histogram by setting different (4 to 12) bits per pixel [18].

Initially, more than 10,000 parameters were determined for each ROI. Subsequently, the parameters that contained NaN values were eliminated. As a result, 10 datasets were generated, corresponding to each ROI, containing a total of 6836 features.

2.5. Statistical Analysis

Statistical analysis was aimed at showing which textural features correlate significantly with age (age distribution presented in Figure 2).
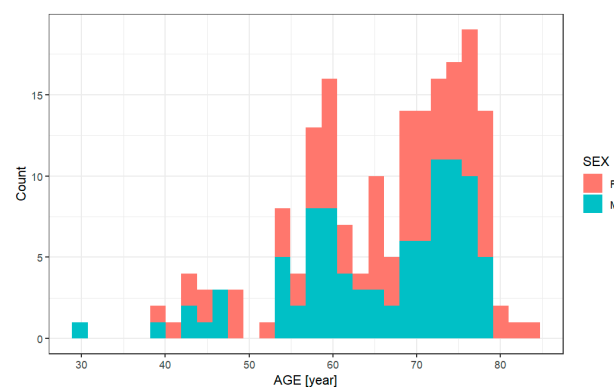

Figure 2. Age distribution, including SEX differences.

In the first step, the Shapiro–Wilk test [20] and Q-Q plot were used to evaluate the distribution of continuous variables. Continuous data were presented as mean (standard deviation, SD) or median (interquartile range, IQR) and compared using Student's *t*-test and Mann–Whitney–Wilcoxon U test, respectively. When one of the subgroups in the study groups had a non-normal type distribution, data were presented as median (IQR) and Mann–Whitney–Wilcoxon U test. Categorical data were presented as numbers (percentages), and Fisher's exact test was used to compare them. This determined the steps for further analysis, which was the calculation of Spearman's Rank correlation or Pearson's coefficient for each ROI. Regression models were used as quantitative methods to assess whether and how the predictor; AGE correlates with the selected textures. Further, mixed-effects regression models were used as an extension of fixed-effects regression models to account for hierarchical data structures (Tables 2 and 3 show comparison results of generated models). Such analysis takes into account intra-individual association between variables because we had a mixed data set; some data were collected for participants at several different time points. LME4 R packages were used to develop mixed-effect models.

Table 2. Summary of standard regression (fixed-effect models) for the most prominent textures.

Model	Variable	Estimate (β Coefficients)	SE	*p*-Value	Adjusted R2	AIC
MODEL_L02_YM6HogO8b4 fixed_regression	AGE	−0.009	0.001	2.4×10^{-14}	0.271	−161.1173
MODEL_L02_YM4GlcmH4DifEntrp Fixed_regression	AGE	−0.002	0.0003	1.55×10^{-13}	0.2565	−602.232

Table 3. Summary of mixed models for the most prominent textures.

Model	Variable	Estimate (β Coefficients)	SE	T	*p*-Value	Lower_2.5	Upper_97.5	AIC
MODEL_L02_YM6HogO8b4 mixed_regression	AGE	−0.008	0.001	−5.444	0	−0.011	−0.005	−159.9161
MODEL_L02_YM4GlcmH4DifEntrp mixed_regression	AGE	−0.002	0.0004	−4.998	0	−0.003	−0.001	−588.468

The idea behind regression analysis is expressed in the equation below where f(x) is the y-value we want to predict, α is the intercept (the point where the regression line crosses the y-axis at x = 0), β is the coefficient (the slope of the regression line).

$$f(x) = \alpha + \beta ix + \epsilon$$

SE is a measure that tells how much the coefficients would vary if the same regression were applied to multiple samples from the same population. Thus, a relatively small SE value indicates that the coefficients will remain very stable if the same regression model is fitted to many different samples with identical parameters. A large SE value, on the other hand, says that the model is variable and not very stable or reliable because the coefficients change substantively if the model is applied to many samples.

$$StandardError(SE) = \frac{\frac{\sum(\overline{x} - x_i)^2}{N-1}}{\sqrt{N}} = \frac{SD}{\sqrt{N}}$$

The equation below represents a formal representation of a mixed-effects regression with varying:

$$f(x) = \alpha i + \beta ix + \epsilon$$

In this model, each level of the random variable has a different intercept and a different slope. So, to predict the value of a data point, it takes the appropriate intercept (model intercept + random effect intercept) and adds the level factor of that random effect multiplied by the value of x.

The inclusion of a random effect structure with random intercepts is justified as the AIC (Akaike Information Criterion) of the model with random intercepts is substantially lower than the AIC of the model without random intercepts. The Akaike Information Criterion is a mathematical method for evaluating how well a model fits the data it was generated from. In statistics, AIC is used to compare different possible models and determine which one is the best fit for the data. The lower the AIC score, the better.

3. Results

Of the 10 anatomical areas analyzed, only ROI L 02 contained features that showed significant correlations (Table 4). The lowest correlation values were obtained when analyzing the ROI L 04 area, whose features describe the texture parameters of the ischium

texture on the left side of the hip joint. The highest value for this area was characterized by the feature YM5Gab8Z4Mag, with a value of only -0.14.

Table 4. Summary of parameters with the highest Spearman's rank correlation coefficient and *p*-value for each ROI.

ROI	Parameter	rho Spearman	*p*-Value
L 01	YD4DwtHaarS4HH	0.35	1.38×10^{-9}
L 02	**YM6HogO8b4**	**-0.52**	**4.95×10^{-14}**
L 03	YS4Gab24H12Mag	-0.27	0.24×10^{-3}
L 04	YM5Gab8Z4Mag	-0.14	0.4×10^{-2}
L 05	YS5GrlmHMGLevNonUn	0.32	1.60×10^{-5}
R 01	YS6GlcmZ5SumAverg	0.26	1.60×10^{-4}
R 02	YLbpCs8n5	0.31	7.54×10^{-5}
R 03	YN8DwtHaarS1HH	0.37	4.62×10^{-6}
R 04	YD4GrlmHRLNonUni	0.17	0.53×10^{-4}
R 05	YN4Gab24Z12Mag	-0.27	0.90×10^{-3}

ROI L 02 was the most prominent, reaching as high as -0.52 in correlation with YM6HogO8b4 texture. The features determined in this area describe the textural parameters of the left femoral neck. The parameters determined in the right femoral neck area were characterized by lower values and did not coincide with the features determined on the left side (YLbpCs8n5: 0.31).

The results for the parameter YM6HogO8b4 are additionally illustrated in Figure 3 and YM4GlcmH4InvDfMom in Figure 4.
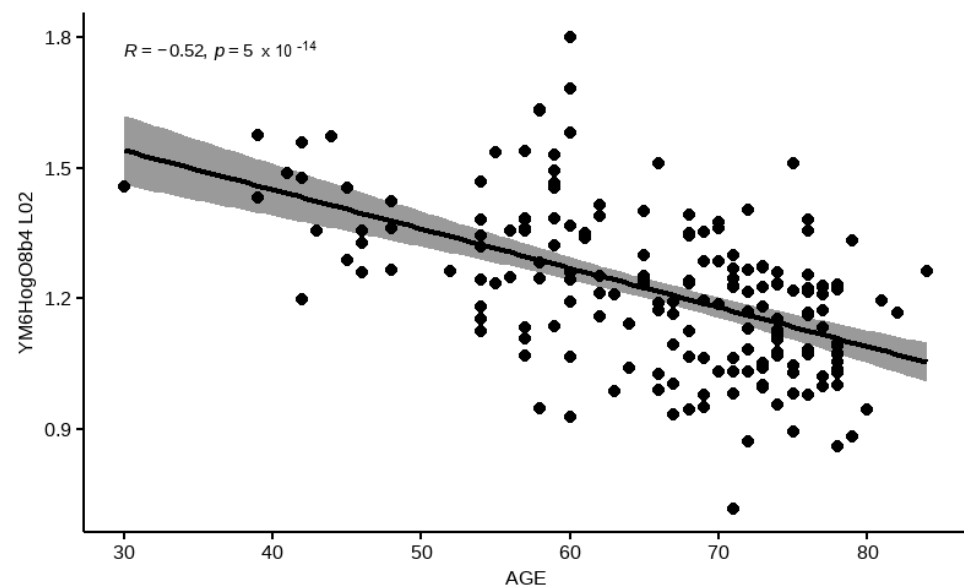

Figure 3. Correlation of YM6HogO8b4 values with age for ROI L 02. The *p*-value of the test is less than the significance level alpha = 0.05; it concludes that age and selected texture are significantly correlated with a correlation coefficient of -0.52 and *p*-value of 5×10^{-14}. This graph shows a negative correlation, which means that every time AGE increases, YM6HogO8b4 values decrease.
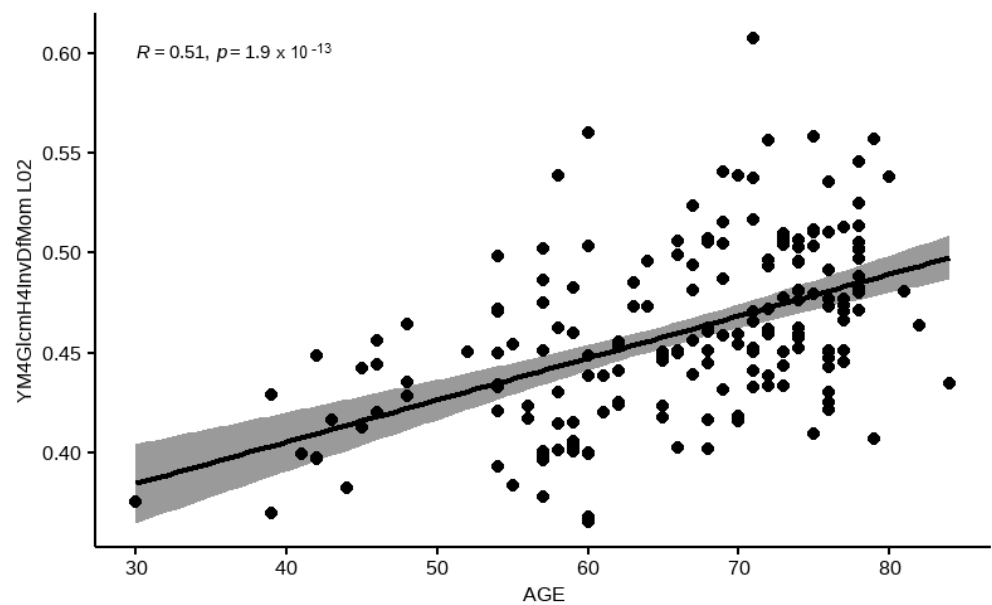
Figure 4. Correlation of YM4GlcmH4InvDfMom values with age for ROI L 02. The *p*-value of the test is less than the significance level alpha = 0.05; it concludes that age and selected texture are significantly correlated with a correlation coefficient of 0.51 and *p*-value of 1.9×10^{-13}. This graph shows a positive correlation. It means that YM4GlcmH4InvDfMom values increase with AGE.

In addition, the most relevant results for ROI L 02 are provided in Table 5.

Table 5. Texture parameters with corresponding rho Spearman correlation results and *p*-values for ROI L 02.

Parameter	rho Spearman	*p*-Value
YM6HogO8b4	−0.5194	4.95×10^{-14}
YM5HogO8b4	−0.5143	9.55×10^{-14}
YM8HogO8b4	−0.5139	1.00×10^{-13}
YM7HogO8b4	−0.5130	1.12×10^{-13}
YM4GlcmH4DifEntrp	−0.5100	1.65×10^{-13}
YM4HogO8b4	−0.5100	1.70×10^{-13}
YM4GlcmH4InvDfMom	0.5088	1.93×10^{-13}
YM4GlcmH4Contrast	−0.5085	1.99×10^{-13}
YM4HogO8b5	−0.5078	2.19×10^{-13}
YM5GlcmH4Contrast	−0.5071	2.38×10^{-13}
YM7GlcmH4Contrast	−0.5070	2.42×10^{-13}

All textural parameters of the femoral neck showing the most significant correlation with age are derived from a histogram of oriented gradients (HOG) or the gray-level co-occurrence matrix (GLCM).

HOG represents an image by calculating the distribution of gradient orientations and magnitudes in small regions of the image called cells. The "8b" in the feature name indicates the number of bins used to create the histogram. The GLCM texture feature proposed by Haralick and Shanmugam [21] is widely recognized as a useful tool for textural feature extraction [22]. It defines how often a combination of pixels occurs in an image by analyzing the spatial relationship between pixels. Another shared feature, including the other ROIs that have been analyzed, is the color component—coded as the first sign Y, which stands for the brightness component from the YUV color space. Another thing worth noting is the recurring last abbreviation defining the descriptor InvDfMom, which stands for Inverse Difference Moment. The higher levels of this parameter represent

an increased pixel uniformity and homogeneity [23]. The meaning of other abbreviations can be retrieved from [18].

4. Discussion

The objective of the current investigation was to establish a relationship between alterations observed in X-ray scans of bones and the age of the individual. Such changes may not be perceptible to the imaging specialist. The utilization of mathematical algorithms to analyze the surrounding pixel environment affords an avenue for examining modifications in the bone microstructure that exceed the capabilities of human vision [24]. Our study focused on establishing correlations between bone structure in varied regions of interest within the proximal femur. X-ray appraisal is a firmly established method for assessing the skeletal system [25].

The high mineral matrix content adjacent to collagen fibrils resists X-ray propagation, which is the basis for determining the bone shape and clinical changes [26]. Bone is a dynamic organ that interacts with the endocrine system to maintain ion equilibrium and acid-base balance. This interaction relies on the action of osteoblasts and osteoclasts, which are differentiated and activated from osteogenic cells (stem cells) progenitors [12]. The lifespan of both cells is relatively short, with osteoblasts and osteoclasts surviving for three months and one month, respectively [27]. The actions of osteoblasts and osteoclasts are necessary for normal bone metabolism, including bone formation and depletion, and for remodeling bone to provide skeletal support, which varies in different locations depending on the load [28].

Although bone remodeling is a continuous process that involves the complete exchange of bone matrix every ten years, the overall bone mass is not significantly decreased [29]. However, advancing age and menopause are significant factors in reducing bone mass [30]. The gradual decrease in osteons and lamellae, as well as the organic and inorganic matrix associated with functional imbalances between osteoclast and osteoblasts, functions that favor osteoclast function, results in a gradual decline in the volume of osteons and overall bone [31]. The decrease in interconnections between bone trabeculae that form lamellae weakens the bone and makes it fragile and susceptible to pathological fractures [32]. This process of bone deterioration is ongoing in both cancellous and compact bone, which is crucial for load transmission [33]. In this study, two regions of interest (ROIs) were analyzed based on correlations of visual-based textural features. One ROI was located in the metaphysis region, where spongy osteocyte-containing bone with complex architecture is present, directed toward withstanding compression and extension forces concentrated along the main axes (lines) of support [34]. The second ROI was located in the peri-trochanteric region, where the compact bone is prevalent.

The peak of bone mass is typically reached after puberty (around 20 years) and gradually declines over one's lifetime [35]. This process, although it can be slowed by physical activity and good dietary habits, is inevitable and cannot be stopped. As trabeculae are overall of lower mass, the effect of the gradual reduction of bone mass is higher in locations with initially smaller bony mass, which is consistent with previous studies on the phenomenon of gradual depletion of bony mass [36]. Such changes are visible on traditional X-rays very late—only a loss of about 30% of the bone mass is visible on X-ray. Dual-energy X-ray absorptiometry (DEXA) is much more sensitive, but it is a less thorough examination and is performed in groups of patients at a certain risk of osteoporosis. The reduction in bone mass in the region of the trochanter is significant due to the influence of estrogen cessation [37]. Estrogens are known to be the most powerful stimuli for inhibiting the action of osteoclasts, which are known for their strong remodeling action on bone [38].

Although, for many years, the reference for diagnostic imaging of bone in humans was the interpretation of a radiologist [25], who is a specialist in diagnostic imaging, the ability of the observer to detect image details does not necessarily reflect the amount of information present in the image [24]. Therefore, many attempts have been made to evaluate bone tissue structure, which is especially susceptible to textural analysis [39]. The idea of using textural

analysis for the evaluation of human tissue visualized in diagnostic imaging techniques is not new. It has been implemented for brain tissue [40–42], breast [43], and even muscle [44]. In the context of bone-based analysis, textural parameters are used, e.g., for the prediction of incident radiographic hip osteoarthritis [45], age-texture correlation analysis [46,47], and association with bone mineral density [48] and bone quality [49].

Contemporary emphasis must be placed on the role of artificial intelligence (AI), in particular deep learning (DL), in the broad field of bone analysis. It is a revolutionary tool that allows researchers to the generation of radiological reports for fractures of the proximal femur [50] and detects fractures directly on the image from different modalities [51–53]. AI-based methods have also demonstrated the potential to predict a patient's age or gender based on images of the bone [54,55]. Furthermore, neural networks can be a valuable support for bone segmentation [56,57] and the detection of a range of bone diseases [58,59].

The textural analysis presents certain benefits when compared to AI. In our theoretical overview, we elucidated the biological basis for changes in bone texture and demonstrated that there are certain specific parameters that are correlated with age. Textual analysis is more suitable for interpretation and, in this particular study, allows us to conclude that the microstructure of bone changes with age, which is accentuated in the images as an increase in the homogeneity and uniformity of pixel values. Furthermore, textural analysis can derive meaningful insights from smaller datasets compared to deep learning. Optional research may be conducted on bone corticalization [60].

This is a relatively new approach as, to the best of our knowledge, there are no similar approaches presented, excluding the work of our team [61] and the work of Dieckmayer [62], who evaluated age among different parameters with the use of deep learning methods; therefore, the approach was very different. Existing works where textures are used for bone assessment are focused on the evaluation of the presence of osteoporosis [63,64]. Textural bone assessment for osteoporosis evaluation was provided on different parts of the skeletal system, such as the jaw [65] and head [66], and with the use of different modalities as CT and MR [67]. Studies on bone mineralization were also evaluated in children [68]. However, bone mineral density was studied already with the use of textural methods, and works where age assessment was performed are lacking; therefore, we assume that our study will have an important contribution to the current literature status.

This study also has several limitations that merit discussion. First, the image acquisition was collected as digitalized images, which may have impacted the quality of the obtained images. In addition, a subset of the acquired images contained endoprostheses, resulting in a lower number of marked regions of interest (ROIs) and possibly affecting the overall distribution of the data. Another limitation of our study was the use of a broad demographic group with the inclusion of extremes of participants' age (youngest and oldest). The demographic is also limited to Caucasian origin with an extended group of participants aged 25–91; however, most of the examined group are above the sixth decade of life. Differences in bone mineral composition may influence the presented results. In future investigations, we aim to conduct more comprehensive analyses on a dataset that does not exhibit the aforementioned limitations and that includes a larger patient cohort.

5. Conclusions

In conclusion, the use of meticulous visual analysis based on textural features of X-ray images was applied, and important correlations of textural features with age were found. Implementation of textural analysis methods proved to be sensitive to changes in bone architecture. The correlation with age found in the bone shaft can be explained by the relatively lower mass of trabecular bone, even in areas of formation of compression supporting lines. The proposed method might be useful in the early diagnosis of osteoporosis. Early diagnosis of changes in bone mechanical strength might be essential in treatment planning and the diagnosis of potential threats associated with bone fragility. The most important statistical correlations were found in the femur neck. This is also the area of the highest clinical importance where most orthopedic urgencies are found. Therefore obtained results

are important from a clinical point of view as they enable us to evaluate accurately areas where a potential bone loss might be a source of serious morbidities and further disabilities for the patient if not properly diagnosed.

Abbreviations

The meaning of texture feature abbreviations used in the article:
e.g., YM4GlcmH4Contrast
#1 {Y}: Y channel of YCbCr—luminance (also for grayscale images)
#2 {D, M, S}: method of normalization—D (no normalization), M—(min-max normalization), S—normalization to $<\mu - 3\sigma, \mu + 3\sigma>$
#3 {8, 7, 6, 5, 4}—number of depth bits (after quantization)
#4 {DwtHaar, Gab, Glcm, Grlm, Hog, Lbp}—texture name
#5 parameters of textures (direction, length}
#6 statistical function—described in detail in [61].

References

1.   Downey, P.A.; Siegel, M.I. Bone Biology and the Clinical Implications for Osteoporosis. *Phys. Ther.* **2006**, *86*, 77–91. [CrossRef] [PubMed]
2.   Holguin, N.; Brodt, M.D.; Sanchez, M.E.; Silva, M.J. Aging Diminishes Lamellar and Woven Bone Formation Induced by Tibial Compression in Adult C57BL/6. *Bone* **2014**, *65*, 83–91. [CrossRef]
3.   Hadjidakis, D.J.; Androulakis, I.I. Bone Remodeling. *Ann. N. Y. Acad. Sci.* **2006**, *1092*, 385–396. [CrossRef] [PubMed]
4.   Gartner, L.P.; Hiatt, J.L. Cartilage and Bone. In *Concise Histology*; Elsevier: Amsterdam, The Netherlands, 2011; pp. 74–93. ISBN 978-0-7020-3114-4.
5.   Rho, J.-Y.; Kuhn-Spearing, L.; Zioupos, P. Mechanical Properties and the Hierarchical Structure of Bone. *Med. Eng. Phys.* **1998**, *20*, 92–102. [CrossRef] [PubMed]
6.   McNally, E.A.; Schwarcz, H.P.; Botton, G.A.; Arsenault, A.L. A Model for the Ultrastructure of Bone Based on Electron Microscopy of Ion-Milled Sections. *PLoS ONE* **2012**, *7*, e29258. [CrossRef]
7.   Huda, W.; Abrahams, R.B. X-ray-Based Medical Imaging and Resolution. *Am. J. Roentgenol.* **2015**, *204*, W393–W397. [CrossRef]
8.   Bonewald, L.F. The Amazing Osteocyte. *J. Bone Miner. Res.* **2011**, *26*, 229–238. [CrossRef]
9.   Parfitt, A.M. Osteonal and Hemi-Osteonal Remodeling: The Spatial and Temporal Framework for Signal Traffic in Adult Human Bone. *J. Cell. Biochem.* **1994**, *55*, 273–286. [CrossRef]
10. Di Girolamo, D.J.; Clemens, T.L.; Kousteni, S. The Skeleton as an Endocrine Organ. *Nat. Rev. Rheumatol.* **2012**, *8*, 674–683. [CrossRef]
11. Noirrit-Esclassan, E.; Valera, M.-C.; Tremollieres, F.; Arnal, J.-F.; Lenfant, F.; Fontaine, C.; Vinel, A. Critical Role of Estrogens on Bone Homeostasis in Both Male and Female: From Physiology to Medical Implications. *Int. J. Mol. Sci.* **2021**, *22*, 1568. [CrossRef]
12. Boskey, A.L.; Coleman, R. Aging and Bone. *J. Dent. Res.* **2010**, *89*, 1333–1348. [CrossRef] [PubMed]
13. Florencio-Silva, R.; da Silva Sasso, G.R.; Sasso-Cerri, E.; Simões, M.J.; Cerri, P.S. Biology of Bone Tissue: Structure, Function, and Factors That Influence Bone Cells. *BioMed Res. Int.* **2015**, *2015*, 421746. [CrossRef] [PubMed]
14. Kerr, D.; Morton, A.; Dick, I.; Prince, R. Exercise Effects on Bone Mass in Postmenopausal Women Are Site-Specific and Load-Dependent. *J. Bone Miner. Res.* **2009**, *11*, 218–225. [CrossRef]
15. Bonjour, J.-P.; Theintz, G.; Law, F.; Slosman, D.; Rizzoli, R. Peak Bone Mass. *Osteoporos. Int.* **1994**, *4*, S7–S13. [CrossRef]

16. Lips, P. Vitamin D Deficiency and Secondary Hyperparathyroidism in the Elderly: Consequences for Bone Loss and Fractures and Therapeutic Implications. *Endocr. Rev.* **2001**, *22*, 477–501. [CrossRef] [PubMed]

17. Khosla, S.; Oursler, M.J.; Monroe, D.G. Estrogen and the Skeleton. *Trends Endocrinol. Metab.* **2012**, *23*, 576–581. [CrossRef]

18. Szczypiński, P.M.; Strzelecki, M.; Materka, A.; Klepaczko, A. MaZda—The software package for textural analysis of biomedical images. In *Computers in Medical Activity*; Advances in Intelligent and Soft Computing; Springer: Berlin/Heidelberg, Germany, 2009; Volume 65, pp. 73–84.

19. Pociask, E.; Nurzynska, K.; Obuchowicz, R.; Bałon, P.; Uryga, D.; Strzelecki, M.; Izworski, A.; Piórkowski, A. Differential Diagnosis of Cysts and Granulomas Supported by Texture Analysis of Intraoral Radiographs. *Sensors* **2021**, *21*, 7481. [CrossRef]

20. Shapiro, S.S.; Wilk, M.B. An Analysis of Variance Test for Normality (Complete Samples). *Biometrika* **1965**, *52*, 591–611. [CrossRef]

21. Haralick, R.M.; Shanmugam, K.; Dinstein, I. Textural Features for Image Classification. *IEEE Trans. Syst. Man Cybern.* **1973**, *SMC-3*, 610–621. [CrossRef]

22. Zhang, H.; Li, Q.; Liu, J.; Shang, J.; Du, X.; McNairn, H.; Champagne, C.; Dong, T.; Liu, M. Image Classification Using RapidEye Data: Integration of Spectral and Textual Features in a Random Forest Classifier. *IEEE J. Sel. Top. Appl. Earth Obs. Remote Sens.* **2017**, *10*, 5334–5349. [CrossRef]

23. Yang, X.; Tridandapani, S.; Beitler, J.J.; Yu, D.S.; Yoshida, E.J.; Curran, W.J.; Liu, T. Ultrasound GLCM Texture Analysis of Radiation-Induced Parotid-Gland Injury in Head-and-Neck Cancer Radiotherapy: An in Vivo Study of Late Toxicity: Ultrasound Assessment of Post-RT Parotid Gland. *Med. Phys.* **2012**, *39*, 5732–5739. [CrossRef] [PubMed]

24. Julesz, B. Experiments in the Visual Perception of Texture. *Sci. Am.* **1975**, *232*, 34–43. [CrossRef]

25. Priolo, F.; Cerase, A. The Current Role of Radiography in the Assessment of Skeletal Tumors and Tumor-like Lesions. *Eur. J. Radiol.* **1998**, *27*, S77–S85. [CrossRef]

26. Fritscher, K.; Grunerbl, A.; Hanni, M.; Suhm, N.; Hengg, C.; Schubert, R. Trabecular Bone Analysis in CT and X-ray Images of the Proximal Femur for the Assessment of Local Bone Quality. *IEEE Trans. Med. Imaging* **2009**, *28*, 1560–1575. [CrossRef] [PubMed]

27. Akkus, O.; Polyakova-Akkus, A.; Adar, F.; Schaffler, M.B. Aging of Microstructural Compartments in Human Compact Bone. *J. Bone Miner. Res.* **2003**, *18*, 1012–1019. [CrossRef]

28. Ammann, P.; Rizzoli, R. Bone Strength and Its Determinants. *Osteoporos. Int.* **2003**, *14*, 13–18. [CrossRef] [PubMed]

29. Bailey, A.J.; Sims, T.J.; Ebbesen, E.N.; Mansell, J.P.; Thomsen, J.S.; Mosekilde, L. Age-Related Changes in the Biochemical Properties of Human Cancellous Bone Collagen: Relationship to Bone Strength. *Calcif. Tissue Int.* **1999**, *65*, 203–210. [CrossRef] [PubMed]

30. Karlamangla, A.S.; Burnett-Bowie, S.-A.M.; Crandall, C.J. Bone Health During the Menopause Transition and Beyond. *Obstet. Gynecol. Clin. N. Am.* **2018**, *45*, 695–708. [CrossRef] [PubMed]

31. Cao, J.J.; Wronski, T.J.; Iwaniec, U.; Phleger, L.; Kurimoto, P.; Boudignon, B.; Halloran, B.P. Aging Increases Stromal/Osteoblastic Cell-Induced Osteoclastogenesis and Alters the Osteoclast Precursor Pool in the Mouse. *J. Bone Miner. Res.* **2005**, *20*, 1659–1668. [CrossRef]

32. Chan, G.K.; Duque, G. Age-Related Bone Loss: Old Bone, New Facts. *Gerontology* **2002**, *48*, 62–71. [CrossRef]

33. Hart, N.H.; Nimphius, S.; Rantalainen, T.; Ireland, A.; Siafarikas, A.; Newton, R.U. Mechanical Basis of Bone Strength: Influence of Bone Material, Bone Structure and Muscle Action. *J. Musculoskelet. Neuronal Interact.* **2017**, *17*, 114–139. [PubMed]

34. Kersh, M.E.; Pandy, M.G.; Bui, Q.M.; Jones, A.C.; Arns, C.H.; Knackstedt, M.A.; Seeman, E.; Zebaze, R.M. The Heterogeneity in Femoral Neck Structure and Strength. *J. Bone Miner. Res. Off. J. Am. Soc. Bone Miner. Res.* **2013**, *28*, 1022–1028. [CrossRef] [PubMed]

35. Riis, B.J.; Hansen, M.A.; Jensen, A.M.; Overgaard, K.; Christiansen, C. Low Bone Mass and Fast Rate of Bone Loss at Menopause: Equal Risk Factors for Future Fracture: A 15-Year Follow-up Study. *Bone* **1996**, *19*, 9–12. [CrossRef] [PubMed]

36. Soldati, E.; Roseren, F.; Guenoun, D.; Mancini, L.; Catelli, E.; Prati, S.; Sciutto, G.; Vicente, J.; Iotti, S.; Bendahan, D.; et al. Multiscale Femoral Neck Imaging and Multimodal Trabeculae Quality Characterization in an Osteoporotic Bone Sample. *Materials* **2022**, *15*, 8048. [CrossRef] [PubMed]

37. Carpenter, R.D.; Sigurdsson, S.; Zhao, S.; Lu, Y.; Eiriksdottir, G.; Sigurdsson, G.; Jonsson, B.Y.; Prevrhal, S.; Harris, T.B.; Siggeirsdottir, K.; et al. Effects of Age and Sex on the Strength and Cortical Thickness of the Femoral Neck. *Bone* **2011**, *48*, 741–747. [CrossRef]

38. Pajamäki, I.; Sievänen, H.; Kannus, P.; Jokihaara, J.; Vuohelainen, T.; Järvinen, T.L.N. Skeletal Effects of Estrogen and Mechanical Loading Are Structurally Distinct. *Bone* **2008**, *43*, 748–757. [CrossRef]

39. Jeong, H.; Kim, J.; Ishida, T.; Akiyama, M.; Kim, Y. Computerised Analysis of Osteoporotic Bone Patterns Using Texture Parameters Characterising Bone Architecture. *Br. J. Radiol.* **2013**, *86*, 20101115. [CrossRef]

40. Kjaer, L.; Ring, P.; Thomsen, C.; Henriksen, O. Texture Analysis in Quantitative MR Imaging. Tissue Characterisation of Normal Brain and Intracranial Tumours at 1.5 T. *Acta Radiol.* **1995**, *36*, 127–135. [CrossRef]

41. Kovalev, V.; Kruggel, F. Texture Anisotropy of the Brain's White Matter as Revealed by Anatomical MRI. *IEEE Trans. Med. Imaging* **2007**, *26*, 678–685. [CrossRef]

42. Mahmoud-Ghoneim, D.; Alkaabi, M.K.; de Certaines, J.D.; Goettsche, F.-M. The Impact of Image Dynamic Range on Texture Classification of Brain White Matter. *BMC Med. Imaging* **2008**, *8*, 18. [CrossRef]

43. Holli, K.; Lääperi, A.-L.; Harrison, L.; Luukkaala, T.; Toivonen, T.; Ryymin, P.; Dastidar, P.; Soimakallio, S.; Eskola, H. Characterization of Breast Cancer Types by Texture Analysis of Magnetic Resonance Images. *Acad. Radiol.* **2010**, *17*, 135–141. [CrossRef] [PubMed]

44. Herlidou, S.; Rolland, Y.; Bansard, J.Y.; Le Rumeur, E.; de Certaines, J.D. Comparison of Automated and Visual Texture Analysis in MRI: Characterization of Normal and Diseased Skeletal Muscle. *Magn. Reson. Imaging* **1999**, *17*, 1393–1397. [CrossRef] [PubMed]

45. Hirvasniemi, J.; Gielis, W.P.; Arbabi, S.; Agricola, R.; van Spil, W.E.; Arbabi, V.; Weinans, H. Bone Texture Analysis for Prediction of Incident Radiographic Hip Osteoarthritis Using Machine Learning: Data from the Cohort Hip and Cohort Knee (CHECK) Study. *Osteoarthr. Cartil.* **2019**, *27*, 906–914. [CrossRef] [PubMed]

46. Mazur, P. The Influence of Bit-Depth Reduction on Correlation of Texture Features with a Patient's Age. In *Progress in Image Processing, Pattern Recognition and Communication Systems*; Choraś, M., Choraś, R.S., Kurzyński, M., Trajdos, P., Pejaś, J., Hyla, T., Eds.; Lecture Notes in Networks and Systems; Springer International Publishing: Cham, Switzerland, 2022; Volume 255, pp. 191–198. ISBN 978-3-030-81522-6.

47. Mazur, P.; Obuchowicz, R.; Piórkowski, A. The Influence of Age on Morphometric and Textural Vertebrae Features in Lateral Cervical Spine Radiographs. In *Information Technology in Biomedicine*; Pietka, E., Badura, P., Kawa, J., Wieclawek, W., Eds.; Advances in Intelligent Systems and Computing; Springer International Publishing: Cham, Switzerland, 2021; Volume 1186, pp. 71–80. ISBN 978-3-030-49665-4.

48. Maciel, J.G.; de Araújo, I.M.; Trazzi, L.C.; de Azevedo-Marques, P.M.; Salmon, C.E.G.; Paula, F.J.A.d.; Nogueira-Barbosa, M.H. Association of Bone Mineral Density with Bone Texture Attributes Extracted Using Routine Magnetic Resonance Imaging. *Clinics* **2020**, *75*, e1766. [CrossRef]

49. Shirvaikar, M.; Huang, N.; Dong, X.N. The Measurement of Bone Quality Using Gray Level Co-Occurrence Matrix Textural Features. *J. Med. Imaging Health Inform.* **2016**, *6*, 1357–1362. [CrossRef] [PubMed]

50. Paalvast, O.; Nauta, M.; Koelle, M.; Geerdink, J.; Vijlbrief, O.; Hegeman, J.H.; Seifert, C. Radiology Report Generation for Proximal Femur Fractures Using Deep Classification and Language Generation Models. *Artif. Intell. Med.* **2022**, *128*, 102281. [CrossRef]

51. Meena, T.; Roy, S. Bone Fracture Detection Using Deep Supervised Learning from Radiological Images: A Paradigm Shift. *Diagnostics* **2022**, *12*, 2420. [CrossRef]

52. Urakawa, T.; Tanaka, Y.; Goto, S.; Matsuzawa, H.; Watanabe, K.; Endo, N. Detecting Intertrochanteric Hip Fractures with Orthopedist-Level Accuracy Using a Deep Convolutional Neural Network. *Skelet. Radiol.* **2019**, *48*, 239–244. [CrossRef] [PubMed]

53. Wang, X.; Xu, Z.; Tong, Y.; Xia, L.; Jie, B.; Ding, P.; Bai, H.; Zhang, Y.; He, Y. Detection and Classification of Mandibular Fracture on CT Scan Using Deep Convolutional Neural Network. *Clin. Oral Investig.* **2022**, *26*, 4593–4601. [CrossRef] [PubMed]

54. Secgin, Y.; Oner, Z.; Turan, M.; Oner, S. Gender Prediction with the Parameters Obtained from Pelvis Computed Tomography Images and Machine Learning Algorithms. *J. Anat. Soc. India* **2022**, *71*, 204. [CrossRef]

55. Zhou, J.; Li, Z.; Zhi, W.; Liang, B.; Moses, D.; Dawes, L. Using Convolutional Neural Networks and Transfer Learning for Bone Age Classification. In Proceedings of the 2017 International Conference on Digital Image Computing: Techniques and Applications (DICTA), Sydney, Australia, 29 November–1 December 2017; pp. 1–6.

56. Cernazanu-Glavan, C.; Holban, S. Segmentation of Bone Structure in X-ray Images Using Convolutional Neural Network. *Adv. Electr. Comput. Eng.* **2013**, *13*, 87–94. [CrossRef]

57. Liu, X.; Han, C.; Wang, H.; Wu, J.; Cui, Y.; Zhang, X.; Wang, X. Fully Automated Pelvic Bone Segmentation in Multiparameteric MRI Using a 3D Convolutional Neural Network. *Insights Imaging* **2021**, *12*, 93. [CrossRef]

58. Eweje, F.R.; Bao, B.; Wu, J.; Dalal, D.; Liao, W.; He, Y.; Luo, Y.; Lu, S.; Zhang, P.; Peng, X.; et al. Deep Learning for Classification of Bone Lesions on Routine MRI. *eBioMedicine* **2021**, *68*, 103402. [CrossRef] [PubMed]

59. He, Y.; Pan, I.; Bao, B.; Halsey, K.; Chang, M.; Liu, H.; Peng, S.; Sebro, R.A.; Guan, J.; Yi, T.; et al. Deep Learning-Based Classification of Primary Bone Tumors on Radiographs: A Preliminary Study. *eBioMedicine* **2020**, *62*, 103121. [CrossRef]

60. Kozakiewicz, M. Measures of Corticalization. *J. Clin. Med.* **2022**, *11*, 5463. [CrossRef]

61. Obuchowicz, R.; Nurzynska, K.; Pierzchala, M.; Piorkowski, A.; Strzelecki, M. Texture Analysis for the Bone Age Assessment from MRI Images of Adolescent Wrists in Boys. *J. Clin. Med.* **2023**, *12*, 2762. [CrossRef]

62. Dieckmeyer, M.; Sollmann, N.; El Husseini, M.; Sekuboyina, A.; Löffler, M.T.; Zimmer, C.; Kirschke, J.S.; Subburaj, K.; Baum, T. Gender-, Age- and Region-Specific Characterization of Vertebral Bone Microstructure Through Automated Segmenta-tion and 3D Texture Analysis of Routine Abdominal CT. *Front. Endocrinol.* **2022**, *12*, 792760. [CrossRef]

63. Lespessailles, E.; Gadois, C.; Kousignian, I.; Neveu, J.P.; Fardellone, P.; Kolta, S.; Roux, C.; Do-Huu, J.P.; Benhamou, C.L. Clinical interest of bone texture analysis in osteoporosis: A case control multicenter study. *Osteoporos. Int.* **2008**, *19*, 1019–1028. [CrossRef]

64. Zheng, K.; Makrogiannis, S. Bone texture characterization for osteoporosis diagnosis using digital radiography. In Proceedings of the 38th Annual International Conference of the IEEE Engineering in Medicine and Biology Society (EMBC), Orlando, FL, USA, 16–20 August 2016; pp. 1034–1037. [CrossRef]

65. Khojastepour, L.; Hasani, M.; Ghasemi, M.; Mehdizadeh, A.R.; Tajeripour, F. Mandibular Trabecular Bone Analysis Using Local Binary Pattern for Osteoporosis Diagnosis. *J. Biomed. Phys. Eng.* **2019**, *9*, 81–88. [CrossRef] [PubMed]

66. Kawashima, Y.; Fujita, A.; Buch, K.; Li, B.; Qureshi, M.M.; Chapman, M.N.; Sakai, O. Using texture analysis of head CT images to differentiate osteoporosis from normal bone density. *Eur. J. Radiol.* **2019**, *116*, 212–218. [CrossRef]

67.   Khider, M.; Taleb-Ahmed, A.; Dubois, P.; Haddad, B. Classification of trabecular bone texture from MRI and CT scan images by multi resolution analysis. In Proceedings of the 29th Annual International Conference of the IEEE Engineering in Medicine and Biology Society, Lyon, France, 22–26 August 2007; pp. 5589–5592. [CrossRef]
68.   Castellanos, N.P.; Martínez, E.; Gutierrez, J. Improving osteoporosis diagnosis in children using image texture analysis. In Proceedings of the 2011 Annual International Conference of the IEEE Engineering in Medicine and Biology Society, Boston, MA, USA, 30 August–3 September 2011. [CrossRef]